Applied Catalysis B: Environmental 283 (2021) 119642

Contents lists available at ScienceDirect

Applied Catalysis B: Environmental

journal homepage: www.elsevier.com/locate/apcatb

Coke formation during high-temperature CO_2 electrolysis over $AFeO_3$ (A = La/Sr) cathode: Effect of A-site metal segregation

Dhruba J. Deka[a], Jaesung Kim[a], Seval Gunduz[a], Deeksha Jain[a], Yingjie Shi[a], Jeffrey T. Miller[b], Anne C. Co[c], Umit S. Ozkan[a,*]

[a] William G. Lowrie Department of Chemical and Biomolecular Engineering, The Ohio State University, USA
[b] Davidson School of Chemical Engineering, Purdue University, 480 Stadium Mall Drive, West Lafayette, IN 47907-2100, USA
[c] Department of Chemistry and Biochemistry, The Ohio State University, USA

ARTICLE INFO

Keywords:
CO_2 electrolysis
Strontium-doped lanthanum ferrite perovskites
Coke formation

ABSTRACT

In this study, strontium-doped lanthanum ferrite perovskite oxides (LSF) with different A-site occupancies were used as cathode catalysts for CO_2 electrolysis at 800 °C. XRD, EXAFS, XPS, FTIR, and temperature-programmed desorption were used to characterize the properties of the material. Fe K-edge EXAFS indicated that oxygen vacancy concentration and oxidation states of Fe atoms increased with concomitant improvement of electronic and ionic conductivities with a decrease in the A-site occupancy. XPS spectra revealed that Sr atoms segregated on the surface of A-site excess LSF92 to a greater degree than that on the A-site deficient LSF72. These segregated A-site metal oxides, especially SrO, are alkaline in nature and hence strongly bind to acidic CO_2 forming stable $SrCO_3$, which consequently facilitates carbon formation. This study highlights the effect of A-site stoichiometric modulation on carbon formation during electrolysis of CO_2, which is crucial for improving the long- term performance of an SOEC.

1. Introduction

High-temperature electrolysis in a solid oxide electrolysis cell (SOEC) is an attractive way of converting CO_2 into fuel and value-added chemicals [1–5]. At the high operating temperatures of such cells ($600-1000\,^{\circ}C$), electric energy demand for CO_2 electrolysis is much lower as compared to that at low temperature, because part of the required energy comes from heat. Higher temperature also leads to faster kinetics with relatively cheaper cathode catalyst materials. This makes SOEC economically more attractive than its low operating temperature counterparts, such as alkaline electrolyzers.

One of the main challenges behind the development of SOEC is designing the cathode catalyst. Due to the high operating temperature, thermally stable materials with a similar coefficient of thermal expansion as the electrolyte is desired. Moreover, the cathode material should have sufficient electronic and oxygen ion conductivity, electrochemical activity, and long-term stability [1]. Various classes of materials such as metal-ceramic composite, perovskite oxide - related structures, and other mixed metal oxides have already been shown to exhibit these properties when used as an SOEC cathode. Among these electrode materials, perovskite oxides show significant potential. Perovskites are mixed metal oxides with a general chemical formula: ABO_3, where A is an alkali or alkaline earth metal and B is a transition metal. A- and B-site doped ferrites (e.g. $La_{0.3}Sr_{0.7}Fe_{0.7}Ti_{0.3}O_3$, $La_{0.6}Sr_{0.4}Fe_{0.8}Ni_{0.2}O_3$, Pd-doped $La_{0.6}Sr_{0.4}Co_{0.2}Fe_{0.8}O_3$, Ce-doped $La_{0.7}Sr_{0.3}Cr_{0.5}Fe_{0.5}O_3$), titanates (e.g. $La_{0.2}Sr_{0.8}TiO_3$, $(La_{0.3}Sr_{0.7})_{0.9}Ti_{0.95}Ni_{0.05}O_3$), chromates (e.g. $(La_{0.75}Sr_{0.25})_{0.27}Cr_{0.5}Mn_{0.5}O_3$) are some examples of perovskites that have been investigated as CO_2 reduction cathodes [1–4,6–17].

Certain modifications of the surface chemical nature of these perovskite oxide cathodes can lead to further improvement of the cell performance. For example, migration of B-site metal ions from a perovskite oxide bulk to the surface of the material forming nanoparticles, a phenomenon known as 'exsolution,' has been shown to significantly enhance the CO_2 reduction activity of perovskite oxide cathodes [1,18]. Exsolution creates oxygen vacancies in the material and the metal nanoparticles improve the specific surface area and conductivity of the electrodes, thereby decreasing the cell resistance and improving the current density. Another problem often experienced at high operating temperatures, which could be solved with surface modification of perovskite oxide, is the weak adsorption of CO_2 on the electrode. CO_2 being a linear molecule lacks polarity at high temperatures, making its adsorption onto the cathode surface difficult. In a recent study, it has been shown that the exsolution of A-site metal oxides such as SrO to the perovskite surface can improve CO_2 adsorption [19]. These metal

---

[*] Corresponding author.
E-mail address: ozkan.1@osu.edu (U.S. Ozkan).

https://doi.org/10.1016/j.apcatb.2020.119642
Received 4 August 2020; Received in revised form 19 September 2020; Accepted 13 October 2020

oxides being alkaline in nature can adsorb CO_2, which is an acidic molecule, with higher binding strength.

The presence of A-site deficiency in the perovskite structure provides a thermodynamic driving force for the exsolution of B-site metal ions [18,20–23]. On the other hand, the presence of A-site excess helps in exsoluting the A-site metal oxides [19,22,24]. As a result, one can find numbers of research articles that study A-site non-stoichiometric (either deficient or excess) perovskites as a potential cathode for high-temperature CO_2 reduction [1]. One phenomenon that can affect the electrochemical performance of a cell, but did not get enough attention in all these studies is the change in A-site segregation on the perovskite surface as a function of A-site stoichiometry. A-site segregation on and near the surface of a perovskite compared to its bulk is a well-known phenomenon [25,26]. It is expected that as A-site stoichiometry increases, the segregation of these ions towards the surface will also increase. Such a change in the availability of A-site metal oxide on the electrode surface can lead to a change in the adsorption of CO_2, and depending on the strength of adsorbed reactant species, carbon or coke might form on the cathode surface.

While most of the studies on perovskite oxide cathode are focused onreducing the cell resistance thereby improving the cell performance, not enough effort has been put into studying the formation of carbon or coke on the electrode surface during electrolysis of CO_2. As mentioned above, increasing the adsorption strength of CO_2 on the electrode surface may have repercussions in terms of coke formation. In addition, when the activity of a cathode increases for CO_2 reduction, there can be coke formation either due to a complete reduction of CO_2 or by the Boudouard reaction initiated by the high concentration of the product CO near the electrode surface. Therefore, it is important to study the effect of A-site stoichiometry not only on CO_2 reduction activity and cell performance, but also on the unintended formation of coke, because the deposition of stable coke can degrade the electrode performance over a period of time.

As already mentioned, ferrite-, titanate- and chromite- based perovskites are being studied as potential cathode materials for high temperature CO_2 reduction. In our earlier publications, we have shown that Ni- and Co-doped lanthanum strontium ferrites can be good cathode candidates for CO_2 reduction [2,17]. However, these studies were focused on the influence of the B-site dopants on the cathode performance. In the current work, we chose lanthanum strontium ferrite as the model SOEC cathode to study the effect of A-site stoichiometry on the cathode properties. Three different compositions of catalysts were used for electrolysis of CO_2: $La_{0.7}Sr_{0.2}FeO_{3-}\delta$ (LSF72), $La_{0.8}Sr_{0.2}FeO_{3-}\delta$ (LSF82), and $La_{0.9}Sr_{0.2}FeO_{3-}\delta$ (LSF92), which are A-site deficient, A-site stoichiometric and A-site excess perovskite oxides, respectively. Here, δ represents the number of oxygen vacancies per formula unit of the perovskite oxide. The effect of the cathode composition on the performance of the electrolysis cell was studied by product gas analysis, current-voltage measurements, and electrochemical impedance measurements. The formation of coke as a function of A-site metal stoichiometry was also investigated. It was found that the presence of A-site deficiency in the perovskite cathode improves the electrochemical performance of the cell. Deposition of coke is observed for the A-site excess cathode LSF92 owing to the greater degree of A-site metal oxide segregation on the surface and higher adsorption of CO_2. In comparison, the A-site deficient cathode LSF72 has a lower A-site concentration on the surface, which helps in avoiding of coke formation during CO_2 electrolysis.

We would like to note that the aim of this paper is not to report on a high-current density cathode electrocatalyst for CO_2 electrolysis, but to explain some of the observed catalytic phenomena such as coking in terms of the changes generated by the compositional variations in the lanthanum strontium ferrites.

2. Experimental section

2.1. *Preparation of materials and catalysts*

Strontium-doped lanthanum ferrites were synthesized via an Ethylenediaminetetraacetic acid (EDTA) -citric acid complexation route with three different compositions: $La_{0.7}Sr_{0.2}FeO_{3-}\delta$ (A-site deficient), $La_{0.8}Sr_{0.2}FeO_{3-}\delta$ (A-site stoichiometric), and $La_{0.9}Sr_{0.2}FeO_{3-}\delta$ (A-site excess). Metal nitrate salts $La(NO_3)_3{\cdot}6H_2O$, $Sr(NO_3)_2$, and Fe $(NO_3)_3{\cdot}9H_2O$ were dissolved in deionized water, and EDTA was added to the solution with an EDTA-to-metal ion molar ratio of 1.5:1 at room temperature, followed by heating. Citric acid was added to the solution with a citric acid-to-metal ion molar ratio of 2:1 at 60 °C, and the temperature was then raised to 90 °C. The pH of the complex solution was adjusted to 6 by the dropwise addition of ammonium hydroxide (NH_4OH) under constant stirring. A viscous gel was formed at the end of this wet-chemistry process, which was then dried at 150 °C for 12 h and ground into a fine powder. This black amorphous precursor was calcined at 1000 °C under air for 5 h to obtain the ferrite perovskite oxide powder denoted as “as-calcined sample”. The term “treated sample” refers to the samples subjected to CO/CO_2 environment and the term “post-reacton sample” refers to the cathode materials after they were used for CO_2 electrolysis as described below.

2.2. *Characterization of As-calcined, CO/CO_2 treated and post-reaction samples*

Powder X-ray diffraction (XRD) patterns were collected in a Bruker D8 Advance X-ray Powder Diffractometer using Cu Kα radiation (40 kV, 40 mA, 0.154 nm) with a step size of 0.014° and dwell time of 0.75 s. General Structure Analysis System-2 (GSAS-2) was used to perform a Rietveld refinement of room temperature patterns to obtain Miller indices of the diffraction peaks [27]. X-ray absorption spectroscopy (XAS) experiments were performed in Sector 10-ID of the Advanced Photon Source of Argonne National Lab. Extended X-ray absorption fine structure (EXAFS) data were subjected to calibration, background correction, normalization, and fitting of the k^2 weighted Fourier transformed EXAFS data in R-space was carried out in the WinXAS software package [28].

Mössbuaer spectra were collected at room temperature and 77 K in a SEE Co. Mössbauer spectrometer using a $^{57}Co/Rh$ γ-ray source. The deconvolution of the Mössbauer spectra was done using Lorentzian line shape in the Fit ;o) software [29]. X-ray photoelectron spectra (XPS) was measured by a Kratos Axis Ultra XPS instrument with a monochromated Mg Kα radiation source (1254.6 eV, 12 kV, 10 mA) and a charge neutralizer at 2.1 A current and 0.8 V bias. The binding energy was calibrated using standard C 1s peak at 284.5 eV during data analysis.

For the measurement of electronic conductivity, sample pellets were prepared using a hydraulic press and sintered at 1300 °C for 5 h under air. The pellets were placed in a furnace with silver wires connected to a Keithley 6182 Nanovoltmeter for the measurement of voltage drop and to a Keithley 6220 Precision Current Source for application of DC current. Oxygen evolution from the perovskite samples was investigated by monitoring the signal of $m/z = 32$ for O_2 with a mass-spectroscope while heating a 50 mg sample (pretreated under 10 % O_2/He at 1000 °C) under 30 ccm He flow.

To investigate the type of carbonate species formed on the samples under a reaction environment, the samples were pretreated with 1.6 % CO + 40 % CO_2/He (approximate composition at 14 mA/cm^2 electrolysis current density) at 800 °C for 5 h and were then characterized by Fourier transform infrared spectroscopy (FTIR), Temperature-programmed desorption (TPD), and XPS analysis. FTIR spectra of the pretreated samples mixed with KBr in a weight ratio of 1:20 were collected at room temperature in a Thermoelectron Nicolet 6700 FTIR instrument equipped with an MCT detector. The $m/z = 44$ signal (for

CO_2) was recorded with a mass-spectroscopy for TPD profile by heating the CO/CO_2 pretreated samples up to 1000 °C at a rate of 10 °C min^{-1} under 30 ccm of helium.

Post-electrolysis cells were examined by their temperature-programmed oxidation (TPO) profile, laser Raman spectroscopy, XPS measurement, and scanning electron microscopy (SEM). All cells were used for CO_2 reduction at 14 mA cm^{-2} for 48 h at 800 °C. TPO profile was collected by monitoring the $m/z = 44$ signal for CO_2 by heating the sample to 1000 °C at a ramp rate of 10 °C min^{-1} under 30 sccm of 10 % O_2/He flow. Laser Raman spectra were collected on a Horiba LabRAM HR-800 Raman Spectrometer at room temperature with a 5 mW argon ion at 514.5 nm as the excitation source. In order to distinguish between the surface and subsurface atomic composition of the post-reaction cathodes, XPS was performed before and after etching the surface of the cathodes. Sputtering was done inside the vacuum chamber by argon ion beam at 2.4 μA current and 4 keV energy for a duration of 3 min for each sample. SEM backscattered electron images were taken in an FEI Apreo instrument at an accelerating voltage of 1 kV and 6.3 pA beam current.

2.3. *Electrochemical CO_2 reduction*

The electrochemical CO_2 reduction was performed on button cells consisting of yttria-stabilized zirconia (YSZ; ESL Electroscience Laboratory) as an electrolyte, a 50/50 wt% mixture of lanthanum strontium manganite and YSZ (LSM-YSZ; ESL Electroscience Laboratory) as an anode, and synthesized LSF catalysts as cathodes. YSZ green tape with 125 microns of thickness was punched out with one inch of outer diameter and sintered at 1450 °C for 2 h under air. A slurry of LSF cathode mixed with ink vehicle (Nexceris) was screen printed onto one side of the YSZ disc and sintered at 1300 °C for 5 h at a ramp rate of 2 °C min^{-1}. LSM-YSZ anode was prepared on the other side of the disc with the same procedure, except for the sintering temperature at 1200 °C. For CO_2 electrolysis, the prepared button cell was sealed onto one side of an alumina tube using a glass seal, and the anode side was open to the atmosphere for the evolution of oxygen. Fabrication of the button cell and the electrochemical activity test setup are shown in Figure S1 and S2 of the supplementary section. 10 sccm of 40 % of CO_2/He flowed into the cathode side at 800 °C, and the outlet of the reactor was connected to a gas chromatograph (Shimadzu 2014) equipped with a pulsed discharge ionization detector (PDHID) for analyzing CO, CO_2, and H_2. Gold wires were attached with gold paste on both sides of electrodes as current collectors, and the cell was connected to a Biologic potentiostat (SP-150) along with current booster (VMP3) for electrochemical measurements. The Faradaic efficiency reported in the results and discussion section is calculated as the ratio of the total moles of supplied electrons to the moles of electrons needed to form the amount of CO detected by the GC.

3. Results and discussion

3.1. *Bulk property characterization*

3.1.1. *X-ray diffraction*

Fig. 1 shows the room-temperature powder XRD patterns of LSF72, LSF82 and LSF92, and the associated Rietveld refinement. All three samples show a perovskite oxide structure without any impurity phase, and the patterns could be matched to that of $La_{0.8}Sr_{0.2}FeO_3$ (JCPDS file no. 35-1480), which has a structure with orthorhombic symmetry. This indicates that pure perovskite phases of both A-site stoichiometric and non-stoichiometric samples could be synthesized with the EDTA-citric acid complexation method adopted for this study. Rietveld refinement results further confirmed the structure of these perovskites to be orthorhombic, which can be pictorially depicted by the crystal structure shown as inset in Fig. 1 (c). The lattice volume increased slightly with an increase in A-site stoichiometry. Such an expansion of the lattice is due to the decrease in the average oxidation state of Fe-ions caused by the excess La^{3+} ions in the perovskite lattice, as Fe-ions with lower oxidation state has larger ionic radii [2]. The crystallite sizes calculated using the Scherrer equation were also found to increase with the increase in A-site stoichiometry, the values being 44 nm for LSF72, 54 nm for LSF82, and 58 nm for LSF92. Thus, even though A-site non-

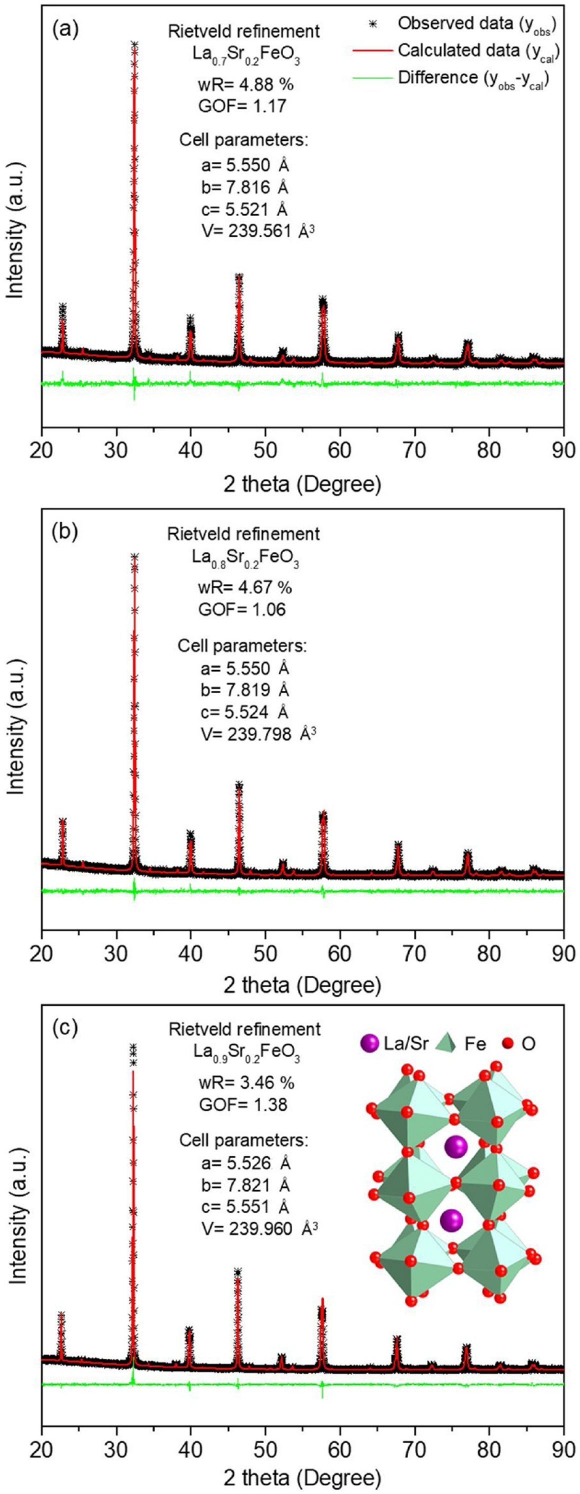

Fig. 1. Rietveld refinement of the X-ray diffractograms of (a) LSF72, (b) LSF82, and (c) LSF92 perovskite oxide powders. Each pattern belongs to an orthorhombic perovskite oxide crystal structure (inset of Fig. 1 (c)). V = Lattice Volume, a/b/c = Lattice Parameters.

Table 1
Fe K-edge EXAFS fitting results: C.N. = Coordination number, R = Fe–O bond distance, σ^2 = Mean square relative displacement or the Debye-Waller factor, ΔE = Energy shift.

Sample	C.N.	R (Å)	σ^2 (Å^2)	ΔE (eV)
LSF92	6 (± 0.1)	1.98 (± 0.0004)	0.001 (± 0.0001)	0.22 (± 0.03)
LSF82	5.9 (± 0.1)	1.98 (± 0.0004)	0.002 (± 0.0001)	0.48 (± 0.03)
LSF72	5.7 (± 0.1)	1.97 (± 0.0002)	0.002 (± 0.00005)	0.37 (± 0.01)

stoichiometry can be successfully realized without disrupting the perovskite structure, it modifies the lattice parameters and crystallite sizes of the samples.

3.1.2. *Extended X-ray absorption fine structure*

Changes in the stoichiometry of the A-site can also change the number of oxygen vacancies present in the material. For example, an A-site deficiency can lead to expulsion of oxygen ions from the perovskite structure to uphold charge neutrality, thereby creating oxygen vacancies. Fe K-edge EXAFS measurements were performed on the ferrite perovskite samples to quantitatively study such oxygen vacancy creation. Figure S3(a)-(c) in the supplementary section show the Fourier transform magnitude of the EXAFS data collected from LSF92, LSF82, and LSF72, respectively, and the fit results of these data are shown in Table 1. The Fe–O bond distance is found to be 1.97–1.98 Å and does not change appreciably among the samples. These bond distances are similar to those reported in the literature for lanthanum strontium ferrite-type materials [30,31]. The first shell surrounding the absorber Fe-atom consists of oxygen atoms. For a perovskite without any oxygen vacancy, this co-ordination is six, leading to the formation of FeO_6 octahedra. However, the oxygen coordination might change depending on the A-site and B-site stoichiometry, oxidation state, and ionic radii of the dopant metal ions. From Table 1, it is observed that the coordination number is 6.0 for LSF92, then decreases with a decrease in A-site occupancy and reaches 5.7 for the A-site deficient sample LSF72. Based on these fit results, the stoichiometric formulae of the perovskite samples can be approximated as $La_{0.7}Sr_{0.2}FeO_{2.85}$ for LSF72, $La_{0.8}Sr_{0.2}FeO_{2.95}$ for LSF82 and $La_{0.9}Sr_{0.2}FeO_{3.0}$ for LSF92. This indicates that the number of inherent oxygen vacancies per formula unit increases with a decrease in A-site occupancy, which is a consequence of the decrease in cationic charge in the material when A-site ions are removed. Some of the oxygen ions must leave the structure to balance these lost cationic charges. Since having oxygen vacancies helps in improving the ionic conductivity, we expect that the ionic conductivity for LSF72 would be higher.

3.1.3. *Mössbauer spectroscopy*

Mössbauer spectroscopy is widely used to differentiate between different species of iron. Mössbauer spectra of LSF72 and LSF92 collected at room temperature are shown in Figure S.4 of the supplementary information. Due to the large broadening and asymmetry of the peaks, it was not possible to deconvolute these spectra. However, it is clear that the spectra for LSF92 have sharper peaks than that for LSF72, indicating that LSF72 crystal structure has a wider distribution of the type of iron species than LFS92 [32,33]. This is caused by the higher degree of distortions and oxygen vacant sites available in LSF72 created by the A-site non-stoichiometry. For a more detailed analysis of the oxidation states of iron, Mössbauer spectra of LSF72, LSF82, and LSF92 were collected at 77 K, which allowed a better S/N due to the slower relaxation of the excited nucleus at low temperature, as shown in Fig. 2. The spectra for LSF72 and LSF82 could be resolved into two sextets with different magnetic hyperfine fields (B_{hf}), quadrupole splitting (QS), and isomeric shifts (IS) as shown in Table 2 and can be assigned to Fe^{3+} and Fe^{5+} species in the perovskite crystal [33,34]. The higher valent iron ions are assigned to Fe^{5+} instead of Fe^{4+} because these tetravalent ions disproportionate into Fe^{3+} and Fe^{5+} at such low temperatures ($Fe^{4+} \leftrightarrow Fe^{3+} + Fe^{5+}$). The spectra for LSF92 contains a contribution from only one sextet that belongs to Fe^{3+}. This indicates that the oxidation state of Fe in the perovskite structure decreases when A-site occupancy is increased and supports similar observations obtained from EXAFS data.

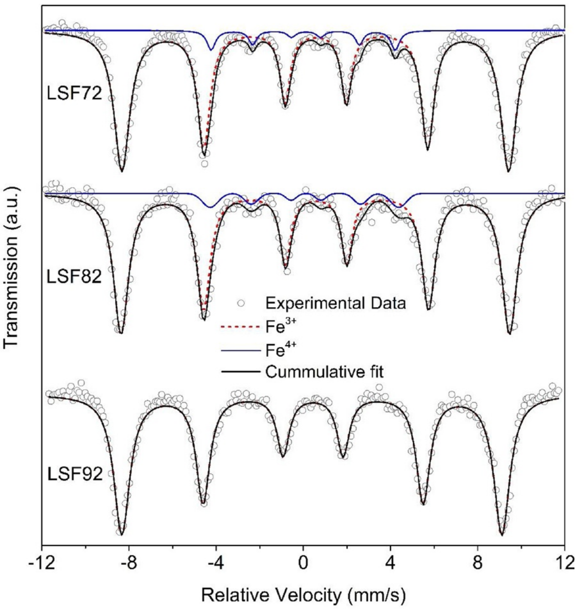

Fig. 2. Mossbauer spectra of LSF72, LSF82 and LSF92 collected at 77 K and associated deconvolution.

Table 2
Parameters obtained by deconvoluting the Mossbauer spectra collected at 77 K.

Sample	Cation	Magnetic Field (B_{hf})	Quadrupole Splitting (QS)	Isomeric Shift (IS)	Intensity (%)
LSF72	Fe^{3+}	55.1	−0.02	0.56	93
	Fe^{5+}	26.3	−0.13	0.05	7
LSF82	Fe^{3+}	55.4	−0.03	0.56	94
	Fe^{5+}	26.9	−0.07	0.08	6
LSF92	Fe^{3+}	54.2	−0.06	0.42	100
	Fe^{5+}	–	–	–	–

3.1.4. *Electronic conductivity*

Fig. 3(a) shows the electronic conductivity of the three samples as a function of temperature. At each test temperature, the electronic conductivity of LSF72 was found to be the highest, and that of LSF92 was found to be the lowest. Lanthanum strontium ferrite perovskites are known to have p-type conductivity, which means that the conductivity in these materials is provided by Fe^{4+}/Fe^{3+} redox couples as charge carriers, as already mentioned. Therefore, higher conductivity can be achieved by having a higher average oxidation state of Fe. Using the room-temperature formulae obtained from the EXAFS results, the oxidation state of Fe can be calculated to be 3.2, 3.1, and 2.9 in LSF72, LSF82, and LSF92, respectively. Having a higher average oxidation state of Fe in LSF72 and a lower average oxidation state in LSF92 leads to the conductivity differences seen here. It is also noted that conductivity initially increases with increasing temperature, then plateaus for LSF72, whereas it decreases for LSF82 and LSF92 with a further increase in temperature. This observation can be explained by the fact that p-type conduction behavior of ferrite perovskites follows the Arrhenius-type equation [35,36]:

$$\sigma = \frac{A}{T}\exp\left(-\frac{E_a}{kT}\right)$$

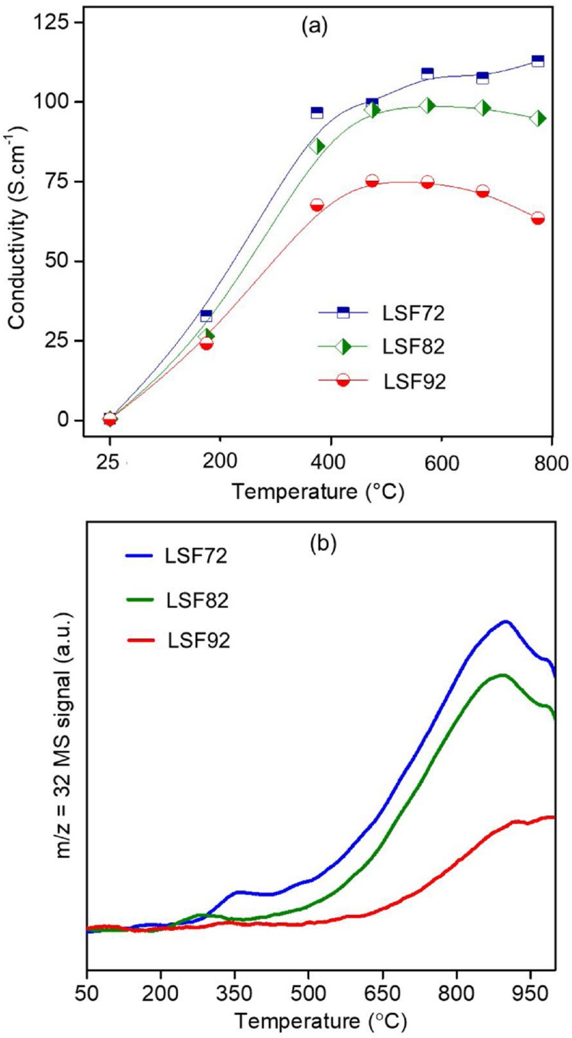

Fig. 3. (a) Electronic conductivity and (b) oxygen vacancy formation as a function of temperature for the samples LSF72, LSF82, and LSF92.

where σ is electronic conductivity, T is temperature, A is a pre-exponential factor, E_a is polaron conduction activation energy, and k is the Boltzmann constant. The Fe^{4+}/Fe^{3+}charge carriers in ferrite perovskites are also known as polarons. At lower temperatures, $E_a > kT$ and hence the conductivity is dominated by the exponential term, which increases with increasing temperatures. At very high temperatures, however, the exponential term becomes smaller compared to the pre-exponential term. The electronic conductivity then depends on the pre-exponential factor (A), which is a function of properties of the material, including charge carrier density [35,36]. At higher temperatures, the creation of oxygen vacancies decreases the oxidation state of the B-site, thereby decreasing the concentration of Fe^{4+}/Fe^{3+} charge carriers. This leads to a decline in the pre-exponential factor and hence the conductivities of the samples. The temperature at which the maximum conductivity occurs (T_{max}) can be predicted for materials exhibiting pure polaron conduction mechanism using the following equation [35]:

$$E_a = k.\ T_{max}$$

The activation energies calculated for LSF72, LSF82, and LSF92 were 0.105 eV, 0.071 eV, and 0.054 eV, respectively, using the Arrhenius-type plot shown in Figure S5. These activation energies predict that the maximum conductivities for LSF72, LSF82, and LSF92 should be achieved at 355 °C, 550 °C, and 945 °C, respectively. Even though the actual temperatures for maximum conductivities were slightly off these calculated values, as seen in Fig. 3(a), the same predicted trend was observed experimentally.

3.1.5. Oxygen vacancy formation

As discussed above, electronic conductivity is dependent on the concnetration of Fe^{4+}/Fe^{3+} redox couples. Higher the number of such charge cariers, higher is the electronic conductivity. In a similar manner, the ionic conductivity of perovskites is a function of the number of oxygen vacancies available in the material. Therefore, quantification of such vacancy formation can be used as an indirect way of comparing ionic conductivities of the samples. Fig. 3(b) shows the m/z = 32 signal (oxygen) as a function of temperature collected during temperature-programmed heating of the samples under helium flow. It can be observed that oxygen is released from the samples with an increase in temperature, and the amount of oxygen evolved increases with a decrease in A-site occupancy. The evolved oxygen was quantified, and the results are shown in Table 3. The number of oxygen atoms evolved per mg (denoted as 'X') of LSF72 at 800 °C is approximately 45 % and 375 % higher than that released from LSF82 and LSF92, respectively. At 1000 °C, this evolved oxygen is still 30 % and 255 % higher for LSF72 than that for LSF82 and LSF92, respectively. The table also shows the oxygen vacancy created per formula unit (denoted as 'δ'), which is the highest for LSF72 and the lowest for LSF92. Thus, A-site deficiency can enhance the oxygen mobility in the perovskite structure, which in turn can improve the oxygen ion conductivity. Starting with the room temperature stochiometric formulae of the samples as obtained from EXAFS fits and considering the oxygen atoms evolved per formula unit (δ), their formulae at an operating temperature of 800 °C can be approximated as $La_{0.7}Sr_{0.2}FeO_{2.82}$ for LSF72, $La_{0.8}Sr_{0.2}FeO_{2.93}$ for LSF82 and $La_{0.9}Sr_{0.2}FeO_{2.99}$ for LSF92. At a higher temperature of 1000 °C, these formulae become $La_{0.7}Sr_{0.2}FeO_{2.79}$ for LSF72, $La_{0.8}Sr_{0.2}FeO_{2.90}$ for LSF82 and $La_{0.9}Sr_{0.2}FeO_{2.98}$ for LSF92. Oxygen evolution at high temperature, therefore, does not change the formula unit to an appreciable extent, which helps in retaining the perovskite oxide crystal structure intact while facilitating oxygen ion transport.

Table 3
Oxygen evolution from ferrite perovskites as a function of temperature. X specifies the cumulative amount of oxygen atoms evolved from RT up to 800 °C, 900 °C and 1000 °C during heat treatment of ferrite perovskite materials under helium flow. δ specifies the oxygen vacancy created per formula unit ($La_xSr_{0.2}FeO_{3}$-δ, x = 0.7, 0.8, or 0.9) during the same temperature periods.

Sample	Amount of O atoms in at RT (μmol/mg)	X = Cumulative evolution of O atoms from RT to T (μmol/mg) δ = Oxygen vacancy formation per formula unit from RT to T							
		T = 25 °C (RT)		T = 800 °C		T = 900 °C		T = 1000 °C	
		X	δ	X	δ	X	δ	X	δ
LSF72	13.181	0	0.15	0.124	0.177	0.197	0.193	0.269	0.208
LSF82	12.731	0	0.05	0.086	0.069	0.147	0.084	0.206	0.098
LSF92	12.176	0	0	0.026	0.006	0.048	0.012	0.076	0.019

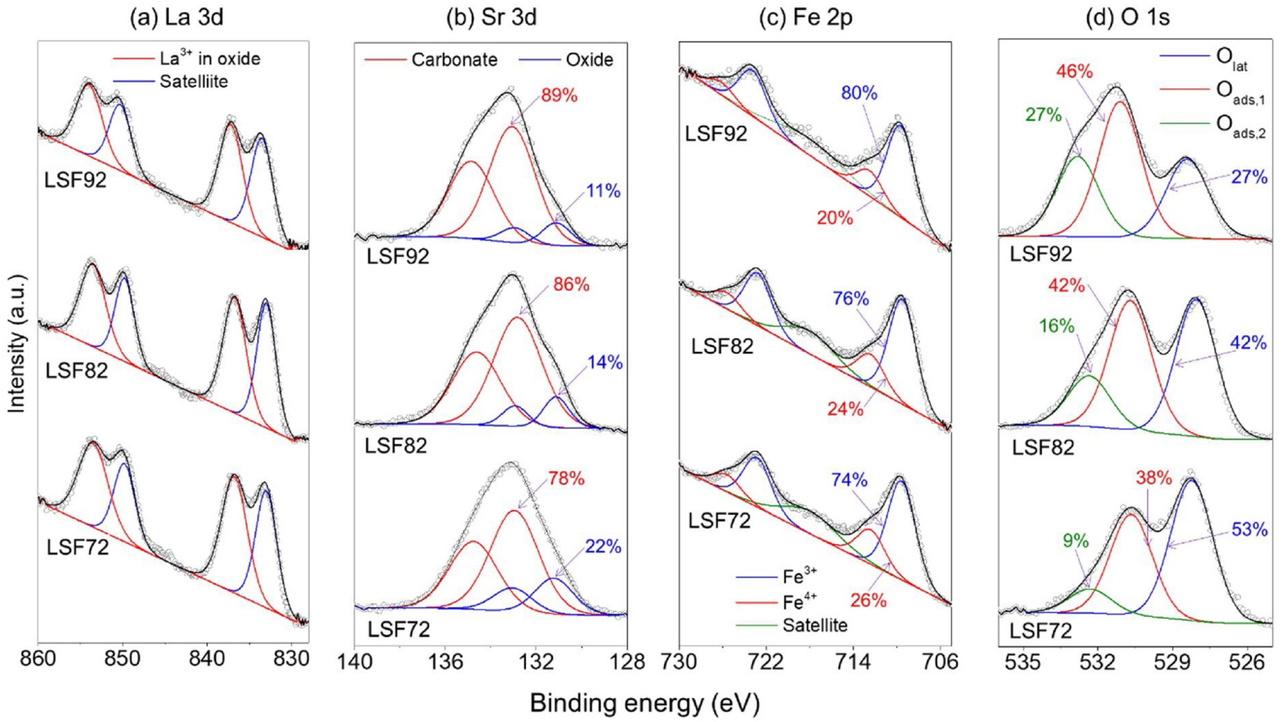

Fig. 4. (a) La 3d, (b) Sr 3d, (c) Fe 2p and (d) O 1s regions of the X-ray photoelectron spectra of as calcined LSF72, LSF82 and LSF92 perovskite powders.

3.2. Surface characterization

3.2.1. X-ray photoelectron spectra

Fig. 4(a)–(d) shows the La 3d, Sr 3d, Fe 2p, and O 1s regions, respectively, of the X-ray photoelectron spectra of as-calcined LSF72, LSF82, and LSF92 samples. La 3d region shows La $3d_{5/2}$ and La $3d_{3/2}$ peaks centered at around 833.3 eV and 850.1 eV, respectively, with a spin-orbit splitting of 16.8 eV. Each of these two transitions is accompanied by a corresponding satellite peak positioned at a 3.7 eV higher binding energy. All these characteristics of the spectra indicate that lanthanum is primarily present in the La^{3+} oxidation state coordinated by an oxide ion environment [2,37]. Fig. 4(b) shows the Sr 3d regions of the three samples. Sr is present as two different species with an oxidation state of +2 in each. The $Sr3d_{5/2}$ peak at 131.2 eV belongs to strontium oxide species, whereas the one at 133.1 eV comes from strontium carbonate species [38,39]. The amount of strontium carbonate species shows an increasing trend as the stoichiometry of the A-site increased. Fe is present at oxidation states of +3 and +4, as shown by the Fe $2p_{3/2}$ peaks at 709.6 eV and 712.4 eV, respectively, in Fig. 4(c) [2]. The overall oxidation state of Fe marginally increases as the A-site stoichiometry is decreased in the order: LSF92, LSF82 and LSF72, as indicated by the increasing contribution from the peak at 712.4 eV. Such an increase in the oxidation state of Fe increases the density of Fe^{4+}/Fe^{3+} redox couples, and since these couples act as charge carriers in p-type conducting perovskites, an improvement in the electronic conductivity of the materials is brought about by A-site deficiency.

Fig. 4(d) shows the O 1s XPS spectra of the three perovskite oxide samples. The deconvolution of these spectra shows the contribution from three oxygen species, which includes the lattice oxygen ion (528.4 eV) and two types of adsorbed oxygen ions (530.9 eV and 532.5 eV) which may be hydroxides and carbonates [26,40]. The percentage of adsorbed oxygen seems to increase with an increase in A-site stoichiometry, which may be a result of the increasing formation of strontium carbonate with the increase in A-site occupancy.

Table 4 shows the relative atomic compositions on the surfaces of LSF72, LSF82, and LSF92. The atomic concentration of oxygen on the surface of each of the three samples is around 70 %, which is higher than the theoretical value of 60 % calculated from the ideal perovskite formula, ABO_3. This oxygen-rich surface is typical of perovskite oxide materials [41,42]. Table 4, in conjunction with Fig. 5, also shows the concentrations of the metal ions and the ratio of A-site ion concentration to B-site ion concentration. Stoichiometrically, LSF72, LSF82, and LSF92 should have La/Fe ratios of 0.7, 0.8, and 0.9, respectively. However, from XPS, these ratios are calculated to be significantly

Table 4
Relative composition of the ferrite perovskite surface calculated from respective XPS spectra.

Sample	Relative Atomic Composition (%)				$\frac{La}{Fe}$	$\frac{Sr}{Fe}$	$\frac{La+Sr}{Fe}$
	La	Sr	Fe	O			
LSF72	6.3	12.7	7.1	73.9	0.9	1.8	2.7
LSF82	6.1	16.3	6.8	70.8	0.9	2.4	3.3
LSF92	7.6	15.3	5.5	71.6	1.4	2.8	4.2

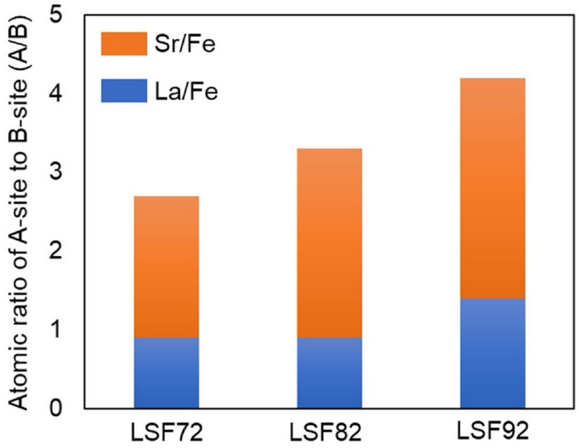

Fig. 5. Ratio of the surface atomic compositions of A-site and B-site metals.

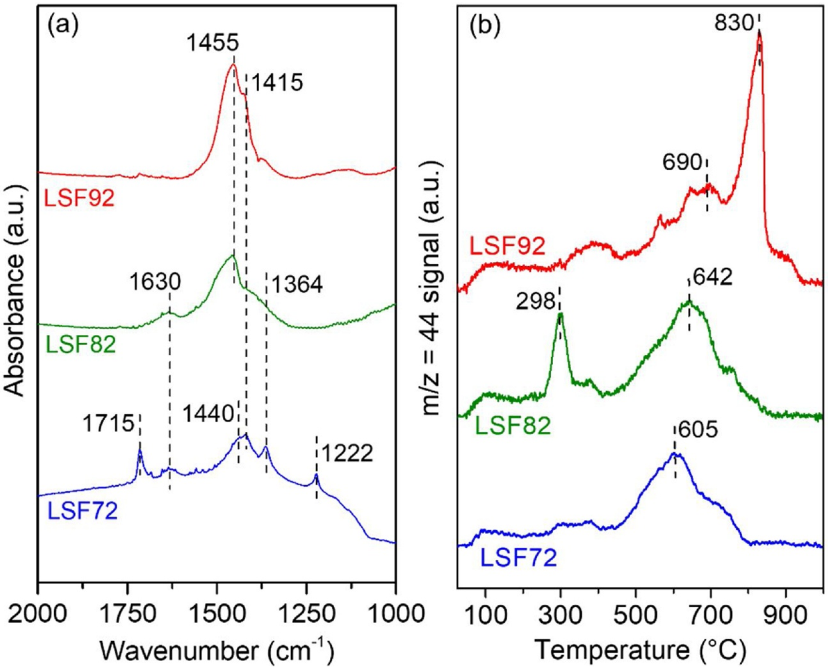

Fig. 6. (a) FTIR spectra, and (b) Temperature- programmed desorption under helium flow of LSF72, LSF82, and LSF92 treated with CO/CO_2 at 800 °C.

higher on the surface. Similarly, Sr/Fe ratios are also much higher on the surface than the average value of 0.2. The overall A-site/B-site {(La + Sr)/Fe} ratios are 2.7, 3.3 and 4.2 for LSF72, LSF82 and LSF92, respectively. These findings show that the surface of these perovskites is rich in the A-site metals. Such surface segregation of the A-site ions is seen to increase with the increase in A-site stoichiometry, i.e., in the order of LSF72, LSF82 and LSF92. An interesting consequence of this phenomenon can be the increase of surface basicity of the ferrite perovskites with an increase in A-site stoichiometry because the A-site metal oxides (e.g., La_2O_3, SrO) are basic in nature. This will result in increased adsorption of the acidic molecule of CO_2, thereby affecting the catalytic activity during CO_2 electrolysis.

3.2.2. Infrared spectroscopy and temperature- programmed desorption

In order to prove this claim, samples of LSF72, LSF82, and LSF92 were exposed to a simulated reaction environment of 1.6 % CO + 40 % CO_2 / He at 800 °C, and the treated samples were then subjected to FTIR and temperature-programmed desorption analysis. FTIR spectra of these treated samples are shown in Fig. 6(a). The band at 1222 cm^{-1} is due to the scissoring mode of COH group in bicarbonate, and the ones at 1630 cm^{-1} and 1715 cm^{-1} can be assigned to the C—O stretching modes of bicarbonate species [43,44]. It is worth mentioning that hydroxyl groups are commonly present on perovskite surfaces due to the adsorption of atmospheric moisture onto the oxygen vacant sites of the material. Since LSF72 has the highest number of oxygen vacancies at any temperature, as shown before, the concentration of adsorbed hydroxyl species is expected to be highest on this sample. That is why, strong bands of bicarbonates formed due to reaction of CO or CO_2 with hydroxyl species are seen on LSF72, which is not the case for LSF82 or LSF92 due to the lower availability of oxygen vacancies. The adsorption bands between 1350–1500 cm^{-1} can be assigned to polydentate carbonate species (CO_3^{2-}), which mainly arise due to the formation of strontium carbonate [45,46]. Because strontium atoms migrate to the surface and their oxide form (SrO) is not stable [19], they readily form stable strontium carbonates ($SrCO_3$) under CO and CO_2 atmosphere. LSF92 has the strongest intensity of the band because the excessive number of A-site atoms (especially Sr) for the stoichiometric number of perovskite (ABO_3) segregate more preferentially to the surface, and have a higher chance of coming in contact with CO and CO_2 molecules than A-site deficient LSF72.

Fig. 6 (b) shows the $m/z = 44$ signal obtained from a mass spectrometer during temperature-programmed heating of the treated samples under helium flow. All three samples show varied signals below 500 °C, which are due to the desorption of weakly adsorbed carbonates. The peaks in the range 600 °C–700 °C are due to strongly adsorbed carbonate species, which shift to higher temperatures in the order LSF72, LSF82 and LSF92. This shows that the adsorption strength of such carbonate species increases with an increase in A-site stoichiometry. Another sharp peak is observed for LSF92 at 830 °C, which is not present in LSF72 and is weak for LSF82. This feature arises due to the desorption of a firmly bound carbonate species [47,48], most likely from the strontium carbonates, as also seen in the FTIR spectra. As mentioned earlier, the surface of A-site excess ferrite perovskite is more basic than the other samples, which leads to stronger adsorption of CO_2. These strongly bound carbonates desorb at higher temperatures when the samples are heated under helium.

3.3. Electrochemical activity for CO_2 reduction

Fig. 7(a) shows the CO production rates during CO_2 electrolysis on the ferrite perovskite cathodes, and Fig. 7(b) shows the Faradaic efficiencies corresponding to these production rates. LSF72 cathode shows the highest CO production rate and hence the highest Faradaic efficiency. Production rates and Faradaic efficiencies are observed to decrease with an increase in A-site occupancy, i.e., in the order of LSF72, LSF82, and LSF92. Interestingly, even though LSF92 leads to the maximum number of adsorbed carbonates under the reaction environment as seen from FTIR and TPD experiments, this cathode shows the lowest Faradaic efficiency for CO formation. This means that not all adsorbed species are converted into CO. It is shown later that this decrease in Faradaic efficiency on LSF92 cathode is due to the formation of coke during electrolysis.

Fig. 7(c) shows the current-voltage relationship obtained from the electrolysis cells during the CO_2 conversion process. The open-circuit voltage (OCV) of the three cells were around 0.16 V. Under the flow of CO_2/He without any reducing gas (such as CO or H_2) in the stream, the OCV values of the cells are decided by the oxygen partial pressure differences between the anode and cathode chambers. When the Nernst

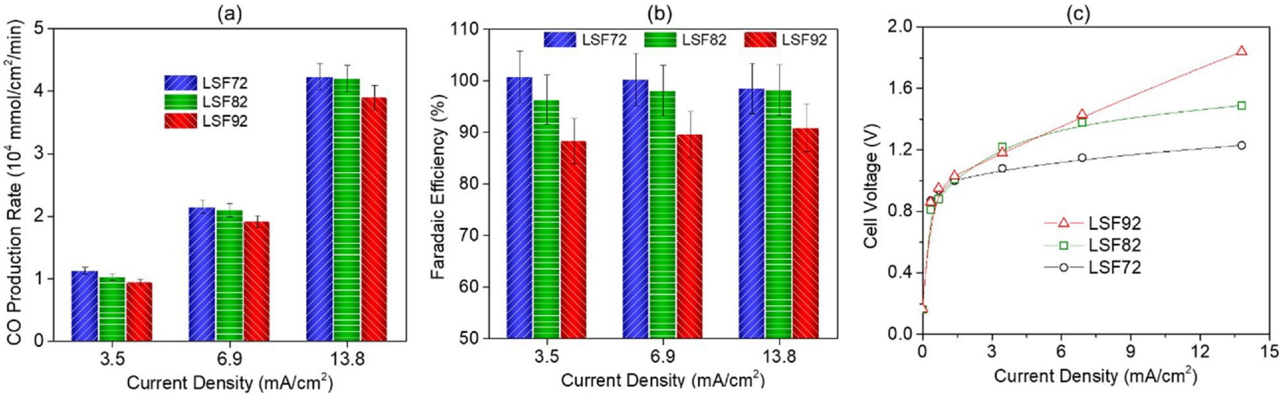

Fig. 7. (a) CO production rates obtained from LSF72, LSF82 and LSF92 cathodes, (b) Faradaic efficiency corresponding to the CO production rates shown in Fig. 7(a), (c) current-voltage relationship obtained during CO_2 electrolysis in cells containing LSF72, LSF82, and LSF92 cathodes. The absolute values of electrolysis current density are used instead of negative current density values for simplicity.

equation is used to calculate the equilibrium cell voltage assuming an oxygen partial pressure of 0.21 atm on the anode side and 10^{-5} atm (0.001 % impurity in the CO_2 cylinder used) on the cathode side, a value of 0.23 V is obtained for 800 °C operating temperature. OCV of around 0.1 V has been reported in the literature where cathode feed streams of CO_2 were used without any reducing gas [2]. At lower current values, there is a steep rise in the I–V curve, and this rate of voltage increase with current gradually decreases at higher current densities. The rapid increase in cell voltage at lower current values is due to kinetic overpotential and activation of the cathode. It is observed that the cell voltage at each current density is the highest for the cell with LSF92 cathode and the lowest for the one with LSF72 cathode. Such an increase of cell voltage for the cell with LSF92 cathode could be due to the lower electronic and ionic conductivity of this material compared to LSF72 or LSF82. Therefore, it can be said that the Faradaic efficiency and electrochemical performance deteriorates when the A-site occupancy of the ferrite perovskite oxide is increased. A-site deficient cathode performs much better than A-site excess cathode due to multiple reasons. The B-site of perovskite is widely regarded as the catalytically active site. A higher atomic percentage of the B-site in the A-site deficient perovskite compared to the A-site excess perovskite makes its activity higher. Moreover, the higher electronic conductivity and oxygen vacant sites make the A-site deficient perovskite a better cathode catalyst. In addition, the presence of the higher amount of segregated $SrCO_3$ on the LSF92 cathode blocks part of the B-site ions, causing its activity to deteriorate.

Fig. 8(a)–(c) shows the Nyquist plots of the electrochemical impedance spectra (EIS) obtained from cells with LSF72, LSF82, and LSF92 cathode, respectively, during CO_2 electrolysis at 800 °C and current densities of 3.5, 6.9 and 13.8 mA/cm^2. The Re(Z)- axis intercept of these EIS curves can be considered as the total resistance of the cells. This total resistance at each current density is observed to be the highest for the cell with LSF92 cathode and the lowest for the cell with LSF72 cathode. This trend is consistent with the observations from the I–V relationships of the electrolysis cells. Impedance for each cell is found to decrease with increasing current density. The EIS plots are observed to be comprised of two semicircular arcs, one at high-frequency values and the other at low-frequency values. An equivalent circuit containing one resistor (R_1) and two resistor-constant phase element circuits (R_2Q_2 and R_3Q_3) in series, as shown inside each of Fig. 8 (a)-(c) was used to fit the EIS data, and the results are tabulated in Table S1. Similar equivalent circuit has been used in other studies in the literature to fit the EIS data collected during CO_2 electrolysis [18,49–52]. Each of the RQ circuits helps in fitting one of the arcs that form the overall EIS. Both the high-frequency resistance (R_2) and the low-frequency resistance (R_3) are found to increase with the increase in the A-site occupancy of the cathode material. The high-frequency arc of the EIS curve arises from charge transfer resistance, and the low-frequency arc comes from the mass transfer and diffusional resistances. Therefore, it can be said that both the charge transfer resistance and mass transfer resistance during CO_2 electrolysis increases with increase in A-site occupancy of the cathode material. Moreover, the table also shows the overall polarization resistance (Rp) of the cells, which increases with an increase in A-site occupancy, indicating better electrochemical performance by the A-site deficient cathode. The polarization resistances for each cell, however, decrease with an increase in

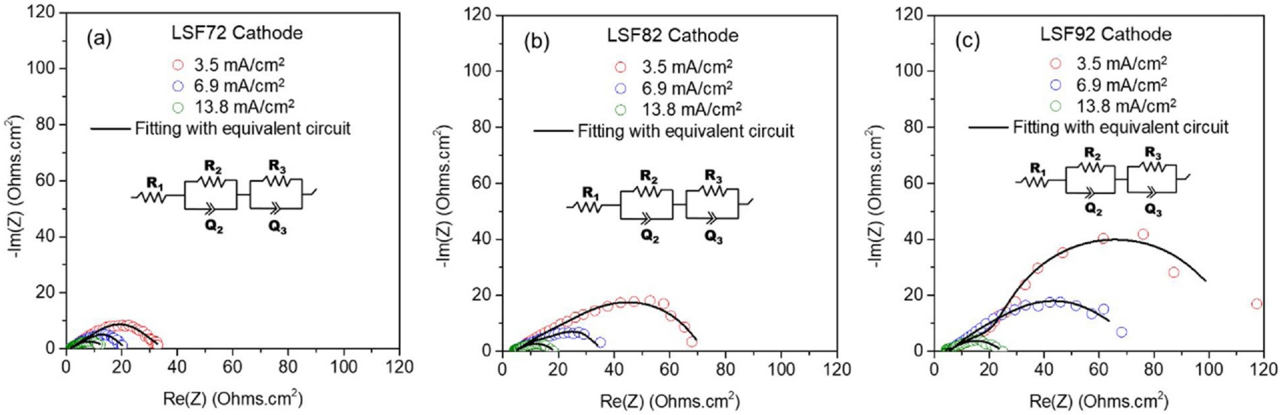

Fig. 8. Nyquist plots of the electrochemical impedance spectra collected during CO_2 electrolysis at 800 °C in cells containing (a) LSF72 cathode, (b) LSF82 cathode, and (c) LSF92 cathode.

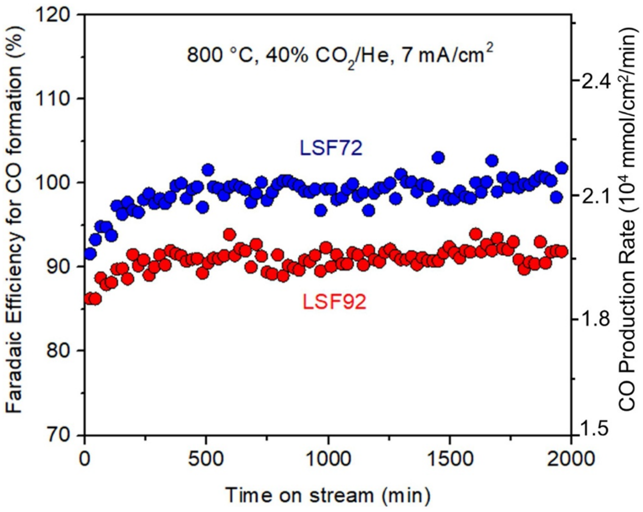

Fig. 9. Faradaic efficiency for CO production during long-term electrolysis test carried out on LSF72 and LSF92 cathodes for approximately 2000 min at a constant current density of 7 mA/cm^2 and operating temperature of 800 °C.

current density, mainly due to the improved kinetics of adsorption and desorption.

Fig. 9 shows the results of a long-term electrolysis experiment performed on LSF72 and LSF92 cathodes at a constant current density of 7 mA/cm^2 and an operating temperature of 800 °C. The cathode feed was a 10 sccm stream of 40 % CO_2/He. The initial rise in the Faradaic efficiency for CO production for both cells is a result of the flow stabilization taking place in the lines connecting the cell outlet and the gas chromatograph as well as stabilization in the GC injections, which needs approximately four hours for the system used in this study, as also mentioned in our earlier studies [2,53]. The Faradaic efficiency for CO production obtained from the LSF72 cathode reached a steady-state value of ca. 100 % while that from LSF92 cathode achieved a steady-state value of 90 %. This lower Faradaic efficiency showcased by the cell with LSF92 cathode indicates that a portion of the electrons supplied to the cell is not being used for CO production. It is shown by post-reaction investigation on the cells that these unaccounted electrons are used for forming coke on the LSF92 cathode over the long operation duration.

3.4. Post-reaction characterization of the cathodes

As mentioned earlier, the Faradaic efficiency for CO formation decreases when LSF92 is used as the cathode as compared to LSF72 cathode. However, since these are constant current experiments, the supplied electrons must be “consumed” to form some other product, if not CO, in the case of LSF92. Therefore, it was suspected that this cathode might form coke during CO_2 electrolysis, which can explain the observed lower Faradic efficiency for CO formation. Post-reaction cells containing LSF72, LSF82, and LSF92 cathodes were subjected to temperature-programmed oxidation (TPO) and Raman spectroscopy experiments for validating this hypothesis. Fig. 10 (a) shows the $m/z = 44$ (CO_2) signal obtained during TPO of the cells under 10 % O_2/ He flow. The peaks at temperatures lower than 500 °C is due to the adsorbed carbonate species. At higher temperatures, no other feature is observed for LSF72 cathode, which means that this material has only the adsorbed carbonates on the surface. LSF82 cathode shows a small peak at 700 °C, which could be due to carbonaceous species. Due to the lower intensity of this peak, we can say that the carbon formed on this cathode is small in quantity. LSF92 cathode, however, shows a strong peak centered around 760 °C and can be assigned to a stable carbon species. These results are also confirmed by the Raman spectra of the post-reaction cathodes shown in Fig. 10 (b). The bands at 1152 cm^{-1} and 1315 cm^{-1} Raman shifts are due to second-order phonon vibrations in the perovskite structure. While the band at 1588 cm^{-1} observed for LSF82 and LSF92 can be assigned to the G-band of carbonaceous species, the peak at 1358 cm^{-1} can be due to the D-band of the same species. The appearance of D and G bands indicates that the stable carbon species shown by the TPO results on LSF92 may be graphitic in nature. It is worth mentioning that the band at 1315 cm^{-1} is not distinct for LSF82 and LSF92, because it may have overlapped with the D-band due to their proximity. From both the TPO and Raman spectroscopy results, it is concluded that LSF92 cathode leads to the formation of coke during CO_2 electrolysis, whereas LSF72 cathode does not.

SEM backscattered images were captured from the post-reaction LSF92 cathode, as shown in Fig. 10 (c). SEM backscattered electron images show Z-contrast, meaning that region of the image that contains lighter elements will appear darker compared to those comprising of heavier elements. The constituent elements for the cathode are La, Sr, and Fe, which are considerably heavier than carbon, and hence any deposited carbon will appear as dark features on the image. From the images shown here, carbon deposition is clearly visible (dark feature) on the cathode surface (brighter region). We could not find any region on the LSF72 cathode with carbon deposition and therefore did not collect any backscattered electron images. A secondary electron SEM image of the LSF72 cathode is shown in Figure S7 showing a clean surface.

While discussing the XPS spectra of LSF72, LSF82, and LSF92 in Fig. 4, it was mentioned that the A-site metal ions, especially Sr, preferentially segregates onto the surface of the perovskite oxide. This segregation was found to be very high for LSF92 and SrO being alkaline in nature accordingly can make the surface of LSF92 more basic in nature. This phenomenon led to higher adsorption of CO_2 on the surface of LSF92, as seen from Fig. 6. Strong adsorption of CO_2 can lead to a complete reduction of the molecule, thereby forming coke. The post-reaction cells were used to carry out X-ray photoelectron spectroscopy experiments to further confirm this argument. Spectra were taken from the post-reaction cathode surface before and after etching with an argon ion gun. Such etching enabled us to find the elemental composition underneath the surface of the cathode. Fig. 12 (a1) and (b1) shows the La 3d spectra before and after etching, respectively. It is observed that there is a contribution from both lanthanum carbonate and oxide to the La 3d spectra collected before etching [54,55]. The presence of lanthanum carbonate is also verified by the entire La 3d region before and after CO_2 electrolysis (without etching) shown in Fig. 11. The spectra after electrolysis are shifted by about 1 eV for all three samples compared to that collected before electrolysis. This shift confirms the presence of a lanthanum carbonate species on the post-electrolysis cathode [54]. Once the surface was etched, lanthanum oxide was the only contributor to the spectra for all three cathodes. Fig. 12 (a2) and (b2) show Sr 3d spectra before and after etching, respectively. The spectra collected before etching show the presence of strontium mainly in the form of strontium carbonate for all the cathodes [38,39]. After etching, however, both strontium oxide and carbonate species are visible in the spectra. The percentage of strontium oxide and strontium carbonate after etching was observed to be a function of the cathode material. In general, the percentage of strontium carbonate increased with an increase in A-site occupancy. Hence, LSF92 cathode showed the highest amount of strontium carbonate after etching. A more quantified representation of these spectra is shown in Fig. 12 (c). This figure shows that all the cathodes contained A-site carbonate species before etching, with LSF92 having the highest percentage of the species (> 90 %). After etching, LSF92 still has around 30 % of these carbonates left, while less than 5 % is found on LSF72 cathode. Therefore, as shown schematically in Fig. 12 (d), we can infer that the A-site excess cathode (LSF92) forms a thicker layer of carbonates on the surface compared to that formed on LSF72.

The formation of A-site carbonate species is also confirmed by the XRD patterns of the post-reaction LSF72, LSF82, and LSF92 cathodes, as

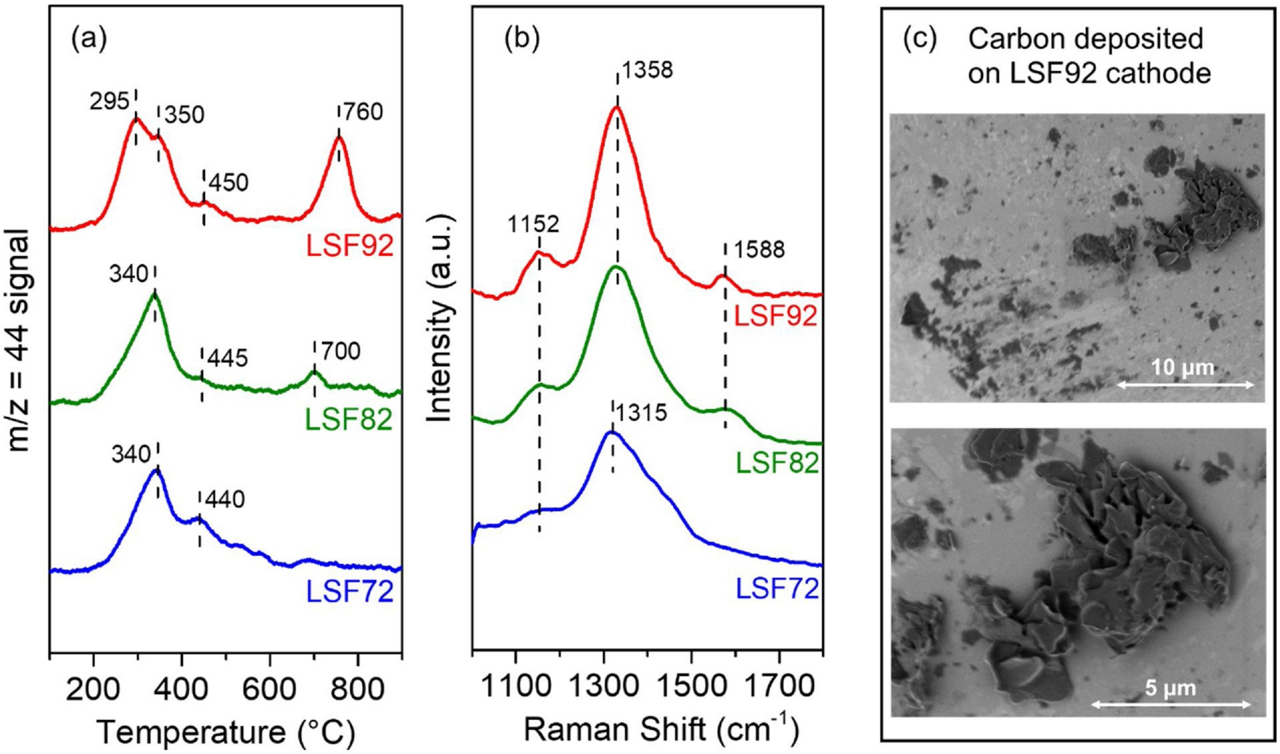

Fig. 10. (a) Temperature- programmed oxidation of post-electrolysis cells under 10 % O_2/He flow, (b) Raman spectra of post-electrolysis LSF cathode, (c) SEM backscattered electron image of the LSF92 cathode after electrolysis showing carbon deposition.

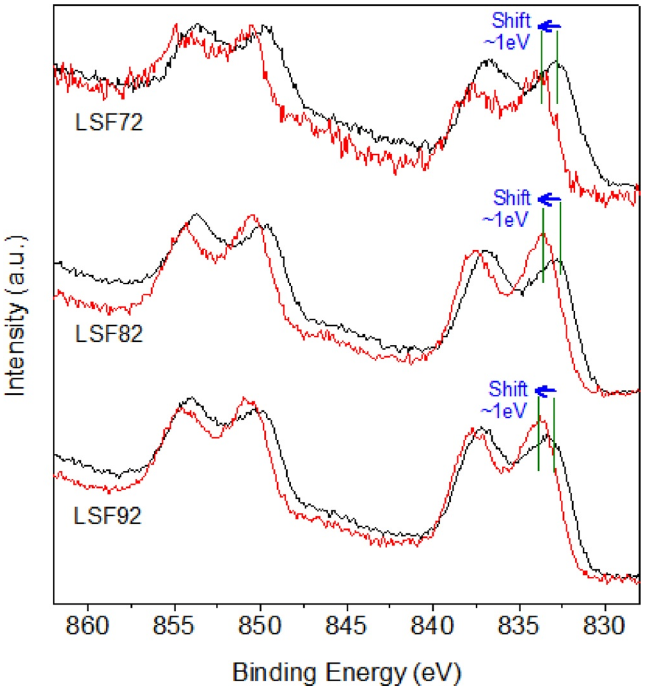

Fig. 11. La 3d XPS spectra collected from the LSF cathodes before (black) and after (red) CO_2 electrolysis operation (For interpretation of the references to colour in this figure legend, the reader is referred to the web version of this article).

shown in Fig. 13. All three cathodes show diffraction lines of $SrCO_3$ (ICDD 71-2393) along with which an additional $La_2O_2CO_3$ phase (ICDD 23-321) is detected on LSF92 cathode. Such carbonate species can lead to the formation of carbon during high-temperature electrolysis of CO_2.

4. Conclusion

In this study, the effect of A-site occupancy of a perovskite oxide cathode on the electrochemical activity for CO_2 reduction is evaluated. A-site deficiency was found to improve the electronic and ionic conductivity of the materials, which also led to improved electrochemical performance. Lower electronic and ionic conductivities of A-site excess cathode resulted in diminished performance. XPS data showed that the A-site ions, especially that of strontium, segregates onto the surface of the material, and such preferential migration increases with an increase in A-site occupancy. SrO being alkaline in nature can adsorb CO_2 more strongly, which is proven by FTIR and temperature-programmed desorption of CO/CO_2 treated samples. XPS of post-electrolysis cathode shows that such stronger interaction of CO_2 with the catalyst surface results in a thicker layer of carbonate on LSF92 cathode compared to LSF72. Stronger adsorbed carbonate can lead to a complete reduction of CO_2 during electrolysis to form carbon. The presence of such carbon was verified by temperature-programmed oxidation, Raman spectroscopy, and SEM results collected from the post-electrolysis cathodes.

CRediT authorship contribution statement

Dhruba J. Deka: Conceptualization, Investigation, Methodology, Data curation, Formal analysis, Writing - original draft. **Jaesung Kim:** Conceptualization, Investigation, Formal analysis, Writing - review & editing. **Seval Gunduz:** Conceptualization, Resources, Validation, Writing - review & editing. **Deeksha Jain:** Investigation. **Yingjie Shi:** Investigation. **Jeffrey T. Miller:** Formal analysis, Writing - review & editing. **Anne C. Co:** Formal analysis, Writing - review & editing. **Umit S. Ozkan:** Conceptualization, Funding acquisition, Project administration, Resources, Supervision, Formal analysis, Writing - review & editing.

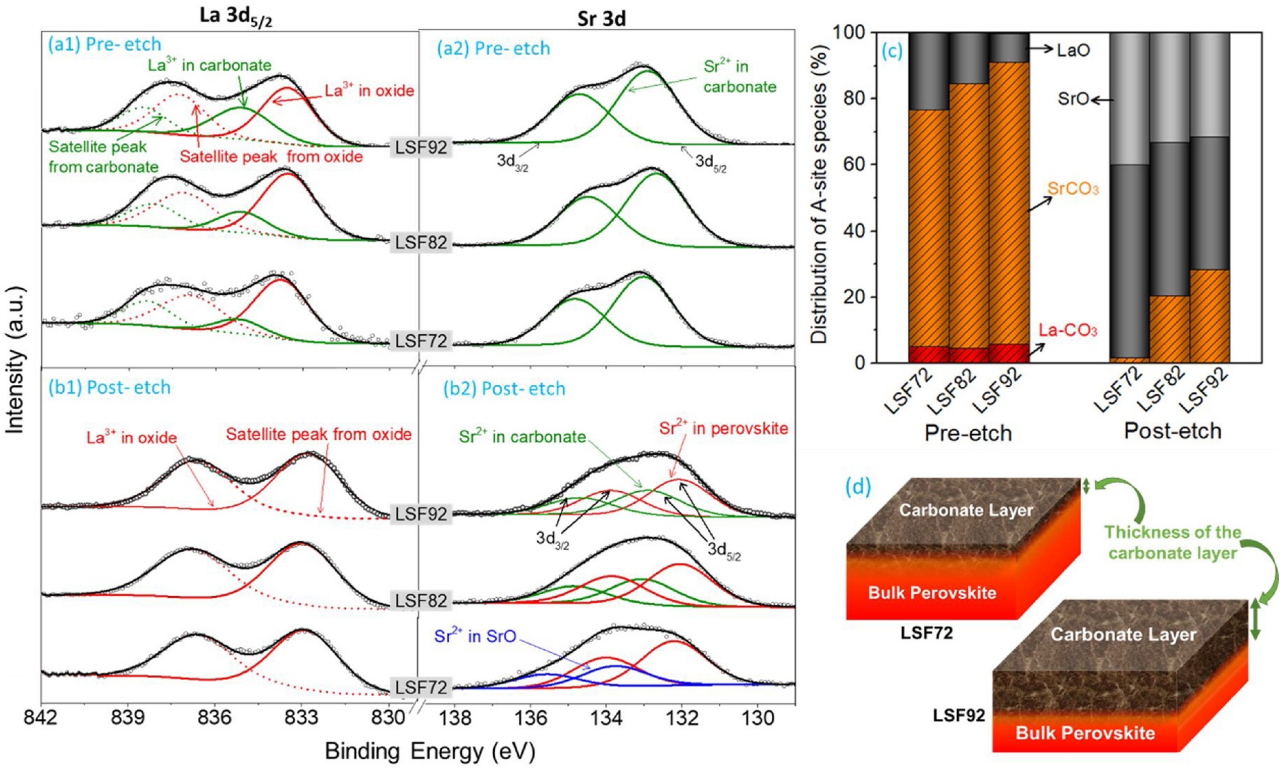

Fig. 12. XPS collected on the post-electrolysis LSF72, LSF82, and LSF92 cathodes before and after etching with argon ion beam: (a1) La 3d5/2 region before etching, (a2) Sr 3d region before etching, (b1) La 3d5/2 after etching, (b2) Sr 3d region after etching, (c) distribution of different La and Sr- species before and after etching, (d) pictorial depiction of the carbonate layer formed on the surface of LSF72 and LSF92 cathode.

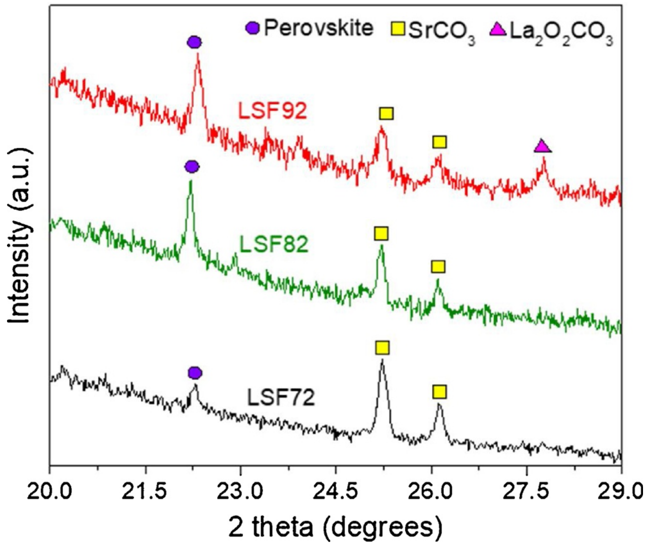

Fig. 13. X-ray diffraction patterns of LSF72, LSF82 and LSF92 cathodes that were subjected to 50 h of CO_2 electrolysis at a current density of 13.8 mA/cm^2 and an operating temperature of 800 °C.

Declaration of Competing Interest

The authors reported no declarations of interest.

Acknowledgments

Financial support provided for this work by the National Science Foundation Division of Chemical, Bioengineering, Environmental and Transport Systems (CBET) under the Award Number GRT00055375 and by the U.S. Department of Energy, Office of Science, Office of Basic Energy Sciences under the Award Number DE-FG02-07ER15896 is gratefully acknowledged. The authors also acknowledge the assistance of Dr. Yehia Khalifa (Surface Analysis Lab, The Ohio State University) on XPS. This research used resources of the Advanced Photon Source, a U.S. Department of Energy (DOE) Office of Science User Facility operated or the DOE Office of Science by Argonne National Laboratory under Contract No. DE-AC02-06CH11357. Assistance from the beamline scientists and staff of sector 10-ID beamline of Materials Research Collaborative Team (MRCAT) at the Advanced Photon Source is acknowledged. J.T. Miller was supported as part of the National Science Foundation Energy Research Center for Innovative and Strategic Transformation of Alkane Resources (CISTAR) under the Cooperative Agreement No. EEC-1647722.

Appendix A. Supplementary data

Supplementary material related to this article can be found, in the online version, at doi:https://doi.org/10.1016/j.apcatb.2020.119642.

References

[1] S. Gunduz, D.J. Deka, U.S. Ozkan, Advances in high-temperature electrocatalytic reduction of CO_2 and H_2O, in: C. Song (Ed.), Advances in Catalysis, Vol. 62 Elsevier Academic Press, Cambridge, 2018, pp. 113–165.

[2] D.J. Deka, S. Gunduz, T. Fitzgerald, J.T. Miller, A.C. Co, U.S. Ozkan, Production of syngas with controllable H_2/CO ratio by high temperature coelectrolysis of CO_2 and H_2O over Ni and Co- doped lanthanum strontium ferrite perovskite cathodes, Appl. Catal. B 248 (2019) 487–503.

[3] L. Zhang, S. Hu, X. Zhu, W. Yang, Electrochemical reduction of CO_2 in solid oxide electrolysis cells, J. Energy Chem. 26 (2017) 593–601.

[4] Y. Zheng, J. Wang, B. Yu, W. Zhang, J. Chen, J. Qiao, J. Zhang, A review of high temperature co-electrolysis of H_2O and CO_2 to produce sustainable fuels using solid oxide electrolysis cells (SOECs): advanced materials and technology, Chem. Soc. Rev. 46 (2017).

[5] A. Cho, J. Ko, B.-K. Kim, J.W. Han, Electrocatalysts with increased activity for coelectrolysis of steam and carbon dioxide in solid oxide electrolyzer cells, ACS

Catal. 9 (2019) 967–976.

[6] K. A.P, S. Giddey, S.P.S. Badwal, Efficient conversion of CO_2 in solid oxide electrolytic cells with Pd doped perovskite cathode on ceria nanofilm interlayer, J. Co2 Util. 17 (2017) 180–187.

[7] F. Bidrawn, G. Kim, G. Corre, J.T.S. Irvine, J.M. Vohs, R.J. Gorte, Efficient reduction of CO_2 in a solid oxide electrolyzer, Electrochem. Solid-State Lett. 11 (2008) B167–B170.

[8] Z. Cao, B. Wei, J. Miao, Z. Wang, Z. Lü, X. Huang, X. Zhu, Q. Feng, Y. Sui, Efficient electrolysis of CO_2 in symmetrical solid oxide electrolysis cell with highly active $La_{0.3}Sr_{0.7}Fe_{0.7}Ti_{0.3}O_3$ electrode material, Electrochem. Commun. 69 (2016) 80–83.

[9] L. Liu, X. Zhou, Y. Wang, S. Li, R. Yin, P. Guo, J. Zhao, X. Zhao, B. Li, Composite ceramic cathode $La_{0.9}Ca_{0.1}Fe_{0.9}Nb_{0.1}O_{3-}\delta$/ $Sc_{0.2}Zr_{0.8}O_{2-}\delta$ towards efficient carbon dioxide electrolysis in zirconia-based high temperature electrolyser, Int. J. Hydrogen Energy 42 (2017) 14905–14915.

[10] S. Liu, Q. Liu, J.-L. Luo, The excellence of $La(Sr)Fe(Ni)O_3$ as an active and efficient cathode for direct CO_2 electrochemical reduction at elevated temperatures, J. Mater. Chem. A 5 (2017) 2673–2680.

[11] J. Lu, S. Li, S. Tao, T. Zhang, K. Xie, Efficient CO_2 electrolysis with scandium doped titanate cathode, Int. J. Hydrogen Energy 42 (2017) 8197–8206.

[12] A.K. Opitz, A. Nenning, C. Rameshan, M. Kubicek, T. Götsch, R. Blume, M. Hävecker, A. Knop-Gericke, Gn. Rupprechter, B. Klötzer, Jr. Fleig, Surface chemistry of perovskite-type electrodes during high temperature CO_2 electrolysis investigated by Operando photoelectron spectroscopy, ACS Appl. Mater. Interfaces 9 (2017) 35847–35860.

[13] Y.-Q. Zhang, J.-H. Li, Y.-F. Sun, B. Hua, J.-L. Luo, Highly active and redox-stable Ce-doped LaSrCrFeO-based cathode catalyst for CO2 SOECs, ACS Appl. Mater. Interfaces 8 (2016) 6457–6463.

[14] Y. Zhou, Z. Zhou, Y. Song, X. Zhang, F. Guan, H. Lv, Q. Liu, S. Miao, G. Wang, X. Bao, Enhancing CO_2 electrolysis performance with vanadium-doped perovskite cathode in solid oxide electrolysis cell, Nano Energy 50 (2018) 43–51.

[15] S. Gunduz, D. Dogu, D.J. Deka, K.E. Meyer, A. Fuller, A.C. Co, U.S. Ozkan, Application of solid electrolyte cells in Ion Pump and electrolyzer modes to promote catalytic reactions: an overview, Catal. Today 323 (2019) 3–13.

[16] D. Dogu, S. Gunduz, K.E. Meyer, D.J. Deka, A.C. Co, U.S. Ozkan, CO_2 and H_2O Electrolysis Using Solid Oxide Electrolyzer Cell (SOEC) with La and Cl- doped Strontium Titanate Cathode, Catal. Letters 149 (2019) 1743–1752.

[17] D.J. Deka, J. Kim, S. Gunduz, M. Ferree, A.C. Co, U.S. Ozkan, Temperature-induced changes in the synthesis gas composition in a high-temperature H2O and CO2 co-electrolysis system, Appl. Catal. A Gen. 602 (2020) 117697.

[18] S. Liu, Q. Liu, J.-L. Luo, Highly stable and efficient catalyst with in situ exsolved Fe–Ni alloy nanospheres socketed on an oxygen deficient perovskite for direct CO_2 electrolysis, ACS Catal. 6 (2016) 6219–6228.

[19] L. Ye, C. Pan, M. Zhang, C. Li, F. Chen, L. Gan, K. Xie, Highly efficient CO_2 electrolysis on cathodes with exsolved alkaline earth oxide nanostructures, ACS Appl. Mater. Interfaces 9 (2017) 25350–25357.

[20] Y. Li, Y. Wang, W. Doherty, K. Xie, Y. Wu, Perovskite chromates cathode with exsolved iron nanoparticles for direct high-temperature steam electrolysis, ACS Appl. Mater. Interfaces 5 (2013) 8553–8562.

[21] Y. Li, K. Xie, S. Chen, H. Li, Y. Zhang, Y. Wu, Efficient carbon dioxide electrolysis based on perovskite cathode enhanced with nickel nanocatalyst, Electrochim. Acta 153 (2015) 325–333.

[22] D. Neagu, G. Tsekouras, D.N. Miller, H. Menard, J.T. Irvine, In situ growth of nanoparticles through control of non-stoichiometry, Nat. Chem. 5 (2013) 916–923.

[23] D.J. Deka, S. Gunduz, J. Kim, T. Fitzgerald, Y. Shi, A.C. Co, U.S. Ozkan, Hydrogen production from water in a solid oxide electrolysis cell: effect of Ni doping on lanthanum strontium ferrite perovskite cathodes, Ind. Eng. Chem. Res. 58 (2019) 22497–22505.

[24] R. Thalinger, M. Gocyla, M. Heggen, B. Klotzer, S. Penner, Exsolution of Fe and SrO Nanorods and Nanoparticles from Lanthanum Strontium Ferrite $La_{0.6}Sr_{0.4}FeO_{3-}\delta$ Materials by Hydrogen Reduction, J. Phys. Chem. C Nanomater. Interfaces 119 (2015) 22050–22056.

[25] J. Druce, H. Tellez, M. Burriel, M.D. Sharp, L.J. Fawcett, S.N. Cook, D.S. McPhail, T. Ishihara, H.H. Brongersma, J.A. Kilner, Surface termination and subsurface restructuring of perovskite-based solid oxide electrode materials, Energy Environ. Sci. 7 (2014) 3593–3599.

[26] W. Jung, H.L. Tuller, Investigation of surface Sr segregation in model thin film solid oxide fuel cell perovskite electrodes, Energy Environ. Sci. 5 (2012) 5370–5378.

[27] B.H. Toby, R.B.V. Dreele, GSAS-II: the genesis of a modern open-source all purpose crystallography software package, J. Appl. Crystallogr. 46 (2013) 544–549.

[28] T. Ressler, WinXAS: A new software package not only for the analysis of energy-dispersive XAS data, Le Journal de Physique IV 7 (1997) 269–270.

[29] J.í. Hjøllum, M.B. Madsen, Fit; o) - A Mossbauer spectrum fitting program, arXiv preprint arXiv (2009) 0912.0449.

[30] T. Montini, M. Bevilacqua, E. Fonda, M.F. Casula, S. Lee, C. Tavagnacco, R.J. Gorte, P. Fornasiero, Relationship between electrical behavior and structural characteristics in Sr-doped $LaNi_{0.6}Fe_{0.4}O_{3-}\delta$ mixed oxides, Chem. Mater. 21 (2009) 1768–1774.

[31] S. Jana, S.K. Panda, D. Phuyal, B. Pal, S. Mukherjee, A. Dutta, P.A. Kumar, D. Hedlund, J. Schött, P. Thunström, Y. Kvashnin, H. Rensmo, M.V. Kamalakar, C.U. Segre, P. Svedlindh, K. Gunnarsson, S. Biermann, O. Eriksson, O. Karis, D.D. Sarma, Charge disproportionate antiferromagnetism at the verge of the insulator-metal transition in doped $LaFeO_3$, Phys. Rev. B 99 (2019) 075106.

[32] H. Yamamura, R. Kiriyama, Oxygen vacancies in the perovskite-type ferrites. II. Mössbauer effect in the SrFeO2. 5-LaFeO3 solid-solution system, Bull. Chem. Soc. Jpn. 45 (1972) 2702–2708.

[33] E. Tsipis, E. Kiselev, V. Kolotygin, J.C. Waerenborgh, V. Cherepanov, V. Kharton, Mixed conductivity, Mössbauer spectra and thermal expansion of (La, Sr)(Fe, Ni) O3− δ perovskites, Solid State Ion. 179 (2008) 2170–2180.

[34] S.E. Dann, D.B. Currie, M.T. Weller, M.F. Thomas, A.D. Al-Rawwas, The effect of oxygen stoichiometry on phase relations and structure in the system La1-xSrxFeO3-δ ($0 \leq x \leq 1$, $0 \leq \delta \leq 0.5$), J. Solid State Chem. 109 (1994) 134–144.

[35] L.-W. Tai, M.M. Nasrallah, H.U. Anderson, D.M. Sparlin, S.R. Sehlin, Structure and electrical properties of $La_{1-x}Sr_xCo_{1-y}Fe_yO_3$. Part 1. The system $La_{0.8}Sr_{0.2}Co_{1-y}FeyO_3$, Solid State Ion. 76 (1995) 259–271.

[36] J.W. Stevenson, T.R. Armstrong, R.D. Carneim, L.R. Pederson, W.J. Weber, Electrochemical properties of mixed conducting perovskites $La_{1-x}M_xCo_{1-y}Fe_yO_{3-}\delta$ (M = Sr, Ba, Ca), J. Electrochem. Soc. 143 (1996) 2722–2729.

[37] A. Machocki, T. Ioannides, D.D.B. Stasinska, W. Gac, W. Grzegorczyk, S. Pasieczna, Manganese–lanthanum oxides modified with silver for the catalytic combustion of methane, J. Catal. 227 (2004) 282–296.

[38] K. Rida, A. Benabbas, F. Bouremmad, M.A. Pena, A. Martinez-Arias, Surface properties and catalytic performance of $La_{1-x}S_rxCrO_3$ perovskite-type oxides for CO and C_3H_6 combustion, Catal. Commun. 7 (2006) 963–968.

[39] E.J. Crumlin, E. Mutoro, Z. Liu, M.E. Grass, M.D. Biegalski, Y.-L. Lee, D. Morgan, H.M. Christen, H. Bluhmg, Y. Shao-Horn, Surface strontium enrichment on highly active perovskites for oxygen electrocatalysis in solid oxide fuel cells†, Energy Environ. Sci. 5 (2012) 6081–6088.

[40] N.A. Merino, B.P. Barbero, P. Eloy, L.E. Cadus, $La_{1-x}Ca_xCoO_3$ perovskite-type oxides: identification of the surface oxygen species by XPS, Appl. Surf. Sci. 253 (2006) 1489–1493.

[41] J.N. Kuhn, U.S. Ozkan, Surface properties of Sr- and Co-doped $LaFeO_3$, J. Catal. 253 (2008) 200–211.

[42] N. Lakshminarayanan, H. Choi, J.N. Kuhn, U.S. Ozkan, Effect of additional B-site transition metal doping on oxygen transport and activation characteristics in $La_{0.6}Sr_{0.4}(Co_{0.18}Fe_{0.72}X_{0.1})O_{3-}\delta$ (where X= Zn, Ni or Cu) perovskite oxides, Appl. Catal. B 103 (2011) 318–325.

[43] J. Rasko, J. Kiss, CO oxidation in the presence of hydrogen on Au/TiO_2 catalyst: an FTIR–MS study, Catal. Lett. 111 (2006) 87.

[44] I.V. Chernyshova, S. Ponnurangam, P. Somasundaran, Linking interfacial chemistry of CO_2 to surface structures of hydrated metal oxide nanoparticles: hematite, Phys. Chem. Chem. Phys. 15 (2013) 6953–6964.

[45] P. Lu, X. Hu, Y. Li, M. Zhang, X. Liu, Y. He, F. Dong, M. Fu, Z. Zhang, One-step preparation of a novel SrCO3/g-C_3N_4 nano-composite and its application in selective adsorption of crystal violet, RSC Adv. 8 (2018) 6315–6325.

[46] Y. Zhu, J. Sunarso, W. Zhou, Z. Shao, Probing CO_2 reaction mechanisms and effects on the $SrNb_{0.1}Co_{0.9-x}Fe_x$O3 cathodes for solid oxide fuel cells, Appl. Catal. B 172-173 (2015) 52–57.

[47] A. Yan, V. Maragou, A. Arico, M. Cheng, P. Tsiakaras, Investigation of a $Ba_{0.5}Sr_{0.5}Co_{0.8}Fe_{0.2}O_3$ based cathode SOFC II. The effect of CO_2 on the chemical stability, Appl. Catal. B 76 (2007) 320–327.

[48] A. Yan, B. Liu, Y. Dong, Z. Tian, D. Wang, M. Cheng, A temperature programmed desorption investigation on the interaction of $Ba_{0.5}Sr_{0.5}Co_{0.8}Fe_{0.2}O_3$ perovskite oxides with CO_2 in the absence and presence of H_2O and O_2, Appl. Catal. B 80 (2008) 24–31.

[49] L. Bian, C. Duan, L. Wang, Y. Hou, L. Zhu, R. O'Hayre, K.-C. Chou, Highly efficient, redox-stable, La0. 5Sr0. 5Fe0. 9Nb0. 1O3-δ symmetric electrode for both solid-oxide fuel cell and H2O/CO2 co-electrolysis operation, J. Electrochem. Soc. 165 (2018) F981.

[50] X. Yue, J.T. Irvine, Impedance studies on LSCM/GDC composite cathode for high temperature CO2 electrolysis, ECS Trans. 41 (2012) 87.

[51] X. Yue, J.T. Irvine, Impedance studies on LSCM/GDC cathode for high temperature CO2 electrolysis, Electrochem. Solid State Lett. 15 (2012) B31.

[52] X. Yue, J.T. Irvine, Alternative cathode material for CO2 reduction by high temperature solid oxide electrolysis cells, J. Electrochem. Soc. 159 (2012) F442.

[53] D. Dogu, K.E. Meyer, A. Fuller, S. Gunduz, D.J. Deka, N. Kramer, A.C. Co, U.S. Ozkan, Effect of lanthanum and chlorine doping on strontium titanates for the electrocatalytically-assisted oxidative dehydrogenation of ethane, Appl. Catal. B 227 (2018) 90–101.

[54] E.A. Lombardo, K. Tanaka, I. Toyoshima, XPS characterization of reduced $LaCoO_3$ perovskite, J. Catal. 80 (1983) 340–349.

[55] G. Sinquin, J.P. Hindermann, C. Petit, A. Kiennemann, Perovskites as polyvalent catalysts for total destruction of C1,C2 and aromatic chlorinated volatile organic compounds, Catal. Today 54 (1999) 107–118.